Comparison of Ensemble Kalman Filter groundwater-data assimilation methods based on stochastic moment equations and Monte Carlo simulation

M. Panzeri [a,*], M. Riva [a,b], A. Guadagnini [a,b], S.P. Neuman [b]

[a] Dipartimento di Ingegneria Civile e Ambientale, Politecnico di Milano, Piazza L. Da Vinci 32, 20133 Milano, Italy
[b] Department of Hydrology and Water Resources, University of Arizona, Tucson, AZ 85721, USA

Received 30 October 2013
Received in revised form 30 January 2014
Accepted 31 January 2014
Available online 10 February 2014

1. Introduction

Kalman Filter (KF) is a well-known inverse technique used to assimilate incoming data into physical system models sequentially in real time. It was originally introduced by Kalman [1] to integrate data corrupted by white Gaussian noise in linear dynamic models the outputs of which include additive noise of a similar type. KF entails two steps: a forward modeling (or forecasting) step that propagates system states in time until new measurements become available, and an updating step that modifies system states optimally in real time on the basis of such measurements. Some modern versions of KF update system states (e.g., hydraulic heads) and parameters (e.g., hydraulic conductivities) jointly based on measurements of one or both variables (e.g., [2]).

Gelb [3] proposed an Extended Kalman Filter (EKF) to deal with nonlinear system models. EKF linearizes the model and propagates the first two statistical moments of target model variables in time. As such it is not suitable for strongly non-linear systems of the kind encountered in the context of groundwater flow or transport in any but mildly heterogeneous media. EKF further requires large amounts of computer storage which limits its use to relatively small-size problems. Evensen [4] and Burgers et al. [5] proposed to overcome these limitations through the use of Monte Carlo (MC) simulation. Their so-called Ensemble Kalman Filter (EnKF) approach utilizes sample mean values and covariances to perform the updating. The development of sensors and measuring devices capable of recording massive amounts of data in real time has made EnKF popular among hydrologists, climate modelers and petroleum reservoir engineers [6,7]; assimilating such massive data sets in batch rather than sequential mode, as is common with classical inverse frameworks such as Maximum Likelihood, would not be feasible. Applications of EnKF to groundwater and multiphase flow problems include the pioneering works of [8,9]; for more recent reviews see [6,7,10].

A crucial factor affecting EnKF is the size of the ensemble, i.e., the number (*NMC*) of MC simulations (sample size) employed for moment evaluation. Whereas to estimate mean and covariance accurately requires many simulations, working with large *NMC* tends to be computationally demanding. Chen and Zhang [11] showed that a few hundred *NMC* appear to provide accurate estimates of mean log-conductivity fields. They pointed out, however, that obtaining covariance estimates of comparable accuracy would require many more simulations, a task they had not carried through. Efforts to reduce the dimensionality of the problem through orthogonal decomposition of state variables have been reported by Zhang et al. [12] and Zeng et al. [13,14].

* Corresponding author. Tel.: +39 0223996256.
E-mail address: marco.panzeri@polimi.it (M. Panzeri).

Small sample sizes give rise to filter inbreeding [6] whereby EnKF systematically understates parameter and system state estimation errors; rather than stabilizing as they should, these errors appear to continue decreasing indefinitely with time, giving a false impression that the quality of the parameter and state estimates likewise keeps improving. There is no general theory to assess, *a priori*, the impact that the number *NMC* of MC simulations would have on the accuracy of moment estimates. The rate at which the sample mean, variance and associated confidence intervals of a random variable converge with the number of Monte Carlo runs is found, for example, in [15] and references therein. It suggests that increasing *NMC* by a factor of a few hundred, as is often done, would likely not lead to marked improvements in accuracy. A practical solution is to continue running MC simulations till the sample mean and variance stabilize or, if computer time is at a premium, till their rates of change slow down markedly.

van Leeuwen [16] showed theoretically that filter inbreeding is caused by (a) updating a given set (ensemble) of model output realizations with a gain computed on the basis of this same set and (b) spurious covariances associated with gains based on finite numbers *NMC* of realizations. Remedies suggested in the literature are generally *ad hoc*. Houtkamer and Mitchell [17] proposed splitting the set of MC runs into two groups and updating each subset with a Kalman gain obtained from the other subset. Hendricks Franssen and Kinzelbach [18] proposed alleviating the adverse effects of filter inbreeding by (a) dampening the amplitude of log-conductivity fluctuations, (b) correcting the predicted covariance matrix on the basis of a comparison between the predicted ensemble variance and the average absolute error at measurement locations, and (c) running a large number of realizations (in their case $NMC = 1000$) during the first simulation step and a subset of realizations ($NMC = 100$) thereafter; a procedure similar to the latter was also suggested in [19]. To select an optimal subset one would minimize some measure of differences between cumulative sample distributions of hydraulic heads obtained in the first step with (say) $NMC = 1000$ and $NMC = 100$. This, however, brings about an artificial reduction in variance [18]. Hendricks Franssen and Kinzelbach [18] obtained best results with a combination of all three techniques. Hendricks Franssen et al. [20] observed filter inbreeding when analyzing variably saturated flow through a randomly heterogeneous porous medium with $NMC = 100$ even after dampening log-conductivity fluctuations by a factor of 10. Several authors (e.g., [21–24]) have seen a reduction in filter inbreeding effects through covariance localization and covariance inflation. Covariance localization is achieved upon multiplying each element of the updated state covariance matrix by an appropriate localization function to reduce the effect of spurious correlations [17,25]. In the covariance inflation methods, the forecast ensemble is inflated through multiplication of each state by a constant or variable factor (e.g., [23,24,26]).

To eliminate the need for repeated MC simulations and associated filter inbreeding effects, we [27] proposed a new EnKF approach based on stochastic moment equations (MEs) of transient groundwater flow [28,29]. Solving these deterministic equations yields direct estimates of theoretical ensemble moments required for EnKF. We tested our new approach on a synthetic two-dimensional flow problem, showing it to yield accurate estimates of log-conductivity and their variance across the flow domain. MEs have been used successfully to analyze steady state [30] and transient flow [29] as well as particle travel times and trajectories [31,32] in randomly heterogeneous media. Second-order approximations of these equations have yielded accurate predictions of flows in heterogeneous media with unconditional variances of (natural) log hydraulic conductivity as high as 4.0 [30]. A transient algorithm based on the Laplace transform due to [29] was shown to be more efficient when computing transient hydraulic head variance than the traditional Monte Carlo method. A detailed comparison between ensemble- and simulation-based inversion methods in the case of steady-state groundwater flow was presented by Hendricks Franssen et al. [33].

While the theoretical elements and the numerical algorithms associated with our new ME-based EnKF framework have been presented in [27], a detailed comparison between MC- and ME-based EnKF variants in domains having various degrees of heterogeneity is still lacking. In this paper we compare the performances and accuracies of these two approaches on synthetic problems of two-dimensional transient groundwater flow toward a well pumping water from a randomly heterogeneous confined aquifer subject to prescribed head and flux boundary conditions. Problems differ from each other in the variance and (integral) autocorrelation scale of the log hydraulic conductivity field. The paper is organized as follows. Section 2 casts the Kalman Filter updating algorithm for groundwater data assimilation within a Bayesian framework (e.g., [34–36]). Section 3 presents the flow problem and describes the two EnKF procedures based on ME and MC. Section 4 illustrates and discusses some of our key results and Section 5 presents our conclusions.

2. Bayesian representations of ME- and MC-based EnKF

We consider transient groundwater flow in a saturated domain Ω governed by stochastic partial differential equations of mass balance and Darcy's law

$$S_S \frac{\partial h(\mathbf{x},t)}{\partial t} + \nabla \cdot \mathbf{q}(\mathbf{x},t) = f(\mathbf{x},t) \tag{1}$$

$$\mathbf{q}(\mathbf{x},t) = -K(\mathbf{x})\nabla h(\mathbf{x},t) \tag{2}$$

subject to initial and boundary conditions

$$h(\mathbf{x},t=0) = H_0(\mathbf{x}) \quad \mathbf{x} \in \Omega \tag{3}$$

$$h(\mathbf{x},t) = H(\mathbf{x},t) \quad \mathbf{x} \in \Gamma_D \tag{4}$$

$$-\mathbf{q}(\mathbf{x},t)\cdot\mathbf{n}(\mathbf{x}) = Q(\mathbf{x},t) \quad \mathbf{x} \in \Gamma_N \tag{5}$$

where $h(\mathbf{x},t)$ is hydraulic head and $\mathbf{q}(\mathbf{x},t)$ the Darcy flux vector at point $(\mathbf{x},t)$ in space–time, $K(\mathbf{x})$ is an autocorrelated random field of scalar hydraulic conductivities, S_S is specific storage treated here as a deterministic constant, $H_0(\mathbf{x})$ is (generally) a random initial head field, $f(\mathbf{x},t)$ is (generally) a random source function of space and time, $H(\mathbf{x},t)$ and $Q(\mathbf{x},t)$ are (generally) random head and normal flux conditions on Dirichlet boundaries Γ_D and Neumann boundaries Γ_N, respectively, and $\mathbf{n}$ is a unit outward normal to Γ_N.

Our goal is to determine the posterior probability distribution of the random augmented (i.e., containing both model parameters and state variables) state vector

$$\mathbf{s} = \begin{bmatrix} \mathbf{Y} \\ \mathbf{h} \end{bmatrix} \tag{6}$$

conditioned on measurements of the random vectors $\mathbf{Y}$ and $\mathbf{h}$. The parameter vector $\mathbf{Y}$ contains N_Y log-conductivities and the state vector $\mathbf{h}$ includes N_h hydraulic head values satisfying (1)–(5), so that $\mathbf{s}$ has dimension $N_s = N_Y + N_h$. In our finite element solver of (1)–(5), described below, N_Y is the number of elements (or collections of elements) in which hydraulic conductivity is taken to be uniform and N_h is the number of nodes at which heads are computed.

We denote the state vector $\mathbf{s}$ at the end of time interval $(T_{k-1}, T_k]$, before new measurements become available at time $t = T_k$, by $\mathbf{s}^{f,T_k}$. In line with [34–36] we consider $\mathbf{s}^{f,T_k}$ to be multivariate Gaussian with *prior* probability density (pdf)

$$f(\mathbf{s}^{f,T_k}) = (2\pi)^{-N_s/2}|\boldsymbol{\Sigma}_{\mathbf{ss}}^{f,T_k}|^{-1/2} \times \exp\left\{-\frac{1}{2}(\mathbf{s}^{f,T_k} - \langle \mathbf{s}^{f,T_k}\rangle)^{+}(\boldsymbol{\Sigma}_{\mathbf{ss}}^{f,T_k})^{-1}(\mathbf{s}^{f,T_k} - \langle \mathbf{s}^{f,T_k}\rangle)\right\} \quad (7)$$

where $\langle\,\rangle$ denotes expectation, the superscript '+' stands for transpose,

$$\langle \mathbf{s}^{f,T_k}\rangle = \begin{bmatrix} \langle \mathbf{Y}^{f,T_k}\rangle \\ \langle \mathbf{h}^{f,T_k}\rangle \end{bmatrix} \quad (8)$$

and

$$\boldsymbol{\Sigma}_{\mathbf{ss}}^{f,T_k} = \langle (\mathbf{s}^{f,T_k} - \langle \mathbf{s}^{f,T_k}\rangle)(\mathbf{s}^{f,T_k} - \langle \mathbf{s}^{f,T_k}\rangle)^{+}\rangle = \begin{bmatrix} \mathbf{C}_Y^{f,T_k} & \mathbf{u}_{Yh}^{f,T_k} \\ \mathbf{u}_{Yh}^{f,T_k+} & \mathbf{C}_h^{f,T_k} \end{bmatrix} \quad (9)$$

is the $N_s \times N_s$ covariance matrix of $\mathbf{s}^{f,T_k}$ in which $\mathbf{C}_Y^{f,T_k}$ and $\mathbf{C}_h^{f,T_k}$ are the covariance matrices of $\mathbf{Y}^{f,T_k}$ and $\mathbf{h}^{f,T_k}$, respectively, and $\mathbf{u}_{Yh}^{f,T_k}$ is their cross-covariance matrix. Suppose that, at time T_k, one measures N_d variables that are linearly proportional to $\mathbf{s}$ where, typically, $N_d \ll N_s$. Denoting this N_d-dimensional vector of measurements by $\mathbf{d}^{T_k}$, the Kalman filter postulates that

$$\mathbf{d}^{T_k} = \mathbf{H}\mathbf{s}^{f,T_k} + \boldsymbol{\varepsilon}_{\mathbf{d}}^{T_k} \quad (10)$$

where $\mathbf{H}$ is a $N_d \times N_s$ transformation matrix (which typically contains numerous zero entries) and $\boldsymbol{\varepsilon}_{\mathbf{d}}^{T_k}$ is a statistically independent vector of Gaussian measurement errors having zero mean and $N_d \times N_d$ covariance matrix $\boldsymbol{\Sigma}_{\boldsymbol{\varepsilon\varepsilon}}^{T_k}$.

The pdf of $\mathbf{d}^{T_k}$, given the prior system states $\mathbf{s}^{f,T_k}$, is the likelihood function

$$f(\mathbf{d}^{T_k}|\mathbf{s}^{f,T_k}) = (2\pi)^{-N_d/2}|\boldsymbol{\Sigma}_{\boldsymbol{\varepsilon\varepsilon}}^{T_k}|^{-1/2} \times \exp\left\{-\frac{1}{2}(\mathbf{d}^{T_k} - \mathbf{H}\mathbf{s}^{f,T_k})^{+}(\boldsymbol{\Sigma}_{\boldsymbol{\varepsilon\varepsilon}}^{T_k})^{-1}(\mathbf{d}^{T_k} - \mathbf{H}\mathbf{s}^{f,T_k})\right\} \quad (11)$$

The *posterior* (updated) pdf of $\mathbf{s}^{f,T_k}$ is related to it through Bayes' theorem according to

$$f(\mathbf{s}^{f,T_k}|\mathbf{d}^{T_k}) = \frac{f(\mathbf{s}^{f,T_k})f(\mathbf{d}^{T_k}|\mathbf{s}^{f,T_k})}{f(\mathbf{d}^{T_k})} \quad (12)$$

where the pdf of $\mathbf{d}^{T_k}$

$$f(\mathbf{d}^{T_k}) = (2\pi)^{-N_d/2}|\boldsymbol{\Sigma}_{\mathbf{dd}}^{T_k}|^{-1/2} \times \exp\left\{-\frac{1}{2}(\mathbf{d}^{T_k} - \langle \mathbf{d}^{T_k}\rangle)^{+}(\boldsymbol{\Sigma}_{\mathbf{dd}}^{T_k})^{-1}(\mathbf{d}^{T_k} - \langle \mathbf{d}^{T_k}\rangle)\right\} \quad (13)$$

plays a normalizing role. From (10) it follows that

$$\langle \mathbf{d}^{T_k}\rangle = \langle \mathbf{H}\mathbf{s}^{f,T_k} + \boldsymbol{\varepsilon}_{\mathbf{d}}\rangle = \mathbf{H}\langle \mathbf{s}^{f,T_k}\rangle \quad (14)$$

$$\boldsymbol{\Sigma}_{\mathbf{dd}}^{T_k} = \langle (\mathbf{d}^{T_k} - \langle \mathbf{d}^{T_k}\rangle)(\mathbf{d}^{T_k} - \langle \mathbf{d}^{T_k}\rangle)^{+}\rangle = \mathbf{H}\boldsymbol{\Sigma}_{\mathbf{ss}}^{f,T_k}\mathbf{H}^{+} + \boldsymbol{\Sigma}_{\boldsymbol{\varepsilon\varepsilon}}^{T_k} \quad (15)$$

Substituting (7), (11), and (13) into (12) allows one to write the *posterior* pdf of the state vector, $\mathbf{s}^{u,T_k}$, as

$$f(\mathbf{s}^{u,T_k}) = f(\mathbf{s}^{f,T_k}|\mathbf{d}^{T_k}) = (2\pi)^{-N_s/2}|\boldsymbol{\Sigma}_{\mathbf{ss}}^{u,T_k}|^{-1/2} \times \exp\left\{-\frac{1}{2}(\mathbf{s}^{u,T_k} - \langle \mathbf{s}^{u,T_k}\rangle)^{+}(\boldsymbol{\Sigma}_{\mathbf{ss}}^{u,T_k})^{-1}(\mathbf{s}^{u,T_k} - \langle \mathbf{s}^{u,T_k}\rangle)\right\} \quad (16)$$

where

$$\langle \mathbf{s}^{u,T_k}\rangle = \langle \mathbf{s}^{f,T_k}\rangle + \mathbf{K}[\mathbf{d}^{T_k} - \mathbf{H}\langle \mathbf{s}^{f,T_k}\rangle] = \begin{bmatrix} \langle \mathbf{Y}^{u,T_k}\rangle \\ \langle \mathbf{h}^{u,T_k}\rangle \end{bmatrix} \quad (17)$$

$$\boldsymbol{\Sigma}_{\mathbf{ss}}^{u,T_k} = (\mathbf{I} - \mathbf{K}\mathbf{H})\boldsymbol{\Sigma}_{\mathbf{ss}}^{f,T_k} = \begin{bmatrix} \mathbf{C}_Y^{u,T_k} & \mathbf{u}_{Yh}^{u,T_k} \\ \mathbf{u}_{Yh}^{u,T_k+} & \mathbf{C}_h^{u,T_k} \end{bmatrix} \quad (18)$$

in which

$$\mathbf{K} = \boldsymbol{\Sigma}_{\mathbf{ss}}^{f,T_k}\mathbf{H}^{+}[\boldsymbol{\Sigma}_{\boldsymbol{\varepsilon\varepsilon}}^{T_k} + \mathbf{H}\boldsymbol{\Sigma}_{\mathbf{ss}}^{f,T_k}\mathbf{H}^{+}]^{-1} \quad (19)$$

is the Kalman gain matrix.

The Bayesian updating procedure embodied in (16)–(19) is common to KF and MC- as well as ME-based EnKF. At this point the three approaches diverge, differing fundamentally in the way each computes the mean and covariance of the prior state vector, $\langle \mathbf{s}^{f,T_k}\rangle$ and $\boldsymbol{\Sigma}_{\mathbf{ss}}^{f,T_k}$. Classical KF computes $\langle \mathbf{s}^{f,T_k}\rangle$ and $\boldsymbol{\Sigma}_{\mathbf{ss}}^{f,T_k}$ on the basis of a linear model the output of which is corrupted by additive Gaussian noise with zero mean and given covariance function (e.g., [10]). We avoid such linearization by updating both log-conductivity and hydraulic head in real-time, as new measurements of one or both of these variables come in, using common MC-based EnKF as well as our new ME-based version [27]. The key steps of the corresponding assimilation procedures are described briefly in Section 3. We treat the forward models as exact, without model error; uncertainty enters through the stochastic nature of our governing equations and through measurement errors.

3. Description of test cases

We consider 9 reference test cases obtained upon solving (1)–(5) in a two-dimensional square domain of 40×40 elements of size 1×1, all quantities being given in consistent space–time units. Each element has uniform hydraulic conductivity, yielding a parameter vector $\mathbf{Y}$ of dimension $N_Y = 1600$. Head values are prescribed or computed at $N_h = 1681$ nodes, yielding a head vector $\mathbf{h}$ of similar dimension. Deterministic head values of 0.8 and 0.0 prescribed along the left and right boundaries, respectively, generate a mean hydraulic gradient of 2% in direction x_1. Top and bottom domain boundaries are set to be impervious (Fig. 1). Initial heads are considered random, as detailed below. Superimposed on this background gradient is convergent flow to a centrally located well that starts pumping at a deterministic constant rate $Q_p = 10^{-3}$ at reference time $t = 0$. Mathematically the well is simulated by setting $f(\mathbf{x}, t = 0) = 0$ and $f(\mathbf{x}, t > 0) = Q_p\,\delta(\mathbf{x} - \mathbf{x}_w)$ in (1) where δ is the Dirac delta function, $\mathbf{x}_w$ are the Cartesian coordinates of the well and well radius is neglected. Storativity is set equal to a uniform deterministic value of 10^{-4}. Nine reference log-conductivity realizations, $Y_{ref}(\mathbf{x}) = \ln K_{ref}(\mathbf{x})$, are generated by

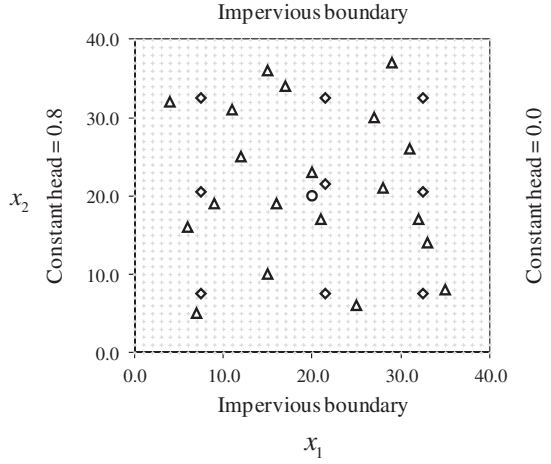

Fig. 1. Flow domain, nodes of the numerical grid (+), boundary conditions, pumping well (○), log-conductivity (◇) and hydraulic head (△) measurement locations.

sampling statistically homogeneous and isotropic multivariate Gaussian fields having mean equal to $ln(10^{-4}) = -9.21$ and 9 exponential variograms with different combinations of sill and integral scale, I_Y, as detailed in Table 1. The reference realizations are generated by the sequential Gaussian simulator SGSIM of Deutsch and Journel [37]. Included in Table 1 are the ratios between domain length scale and I_Y, sample variance, as well as sill and integral scale obtained for each reference realization by fitting, via least squares, an exponential variogram model to the corresponding sample variogram. The least squares variogram parameter estimates are seen to differ, generally, from their original field values.

Both MC- and ME-based EnKF require specifying the variogram parameters for the initial step. We work with the generating rather than the estimated sill and integral scale to avoid introducing additional sources of bias or uncertainty in the comparison. Chen and Zhang [11] showed that incorrect initial sill and integral scale of Y have only a secondary effect on the final log-conductivity estimates. On the other hand, Jafarpour and Tarrahi [38] found in analyzing flow through a highly anisotropic system that inaccuracies in prescribed directional integral scales tends to persist throughout MC-based EnKF runs. The analysis of this effect in the context of ME-based EnKF is outside the scope of the present contribution.

We solve equations (1)–(5) in Laplace transformed form for the duration of 200 time units by the Galerkin finite element method with bilinear Lagrange interpolation functions. We then back transform our solution into the time domain using the quotient difference algorithm of [39]. We sample each reference Y field in nine elements uniformly distributed (Y_m, $m = 1,\ldots 9$) across the domain and the reference head fields at 20 grid points (Fig. 1) and 10 observation times ($h_n^{T_k}$, $n = 1,\ldots 20$, $T_k = 10.0$; 15.0; 20.0; 25.0; 30.0; 50.0; 80.0; 100.0; 150.0; 200.0; $k = 1, 2, ..., 10$). This selection of observation times enables us to sample transient as well as pseudo steady state flow regimes (during which computed heads vary linearly with log time) the latter of which develop, in our cases, at $T_k > 80$. To turn these log-conductivity and head samples into our measurement dataset, we corrupt them with white Gaussian noise, ε_m and $\varepsilon_n^{T_k}$, having zero mean and standard deviations $\sigma_{YE} = 0.1$ and $\sigma_{hE} = 0.01$, respectively, according to

$$Y_m^* = Y_m + \varepsilon_m, \quad m = 1,\ldots,9 \tag{20}$$

$$h_n^{*,T_k} = h_n^{T_k} + \varepsilon_n^{T_k}, \quad n = 1,\ldots,20, \quad k = 1,\ldots,10 \tag{21}$$

The resulting absolute relative differences between reference and measured values range from 0.0% to 2.6% (with mean 0.8%, mode 1.7%, 5th percentile 0.2% and 95th percentile 21.5%) for log-conductivity and from 0.0% to 144% (with mean 4.6%, mode 0.6%, 5th percentile 0.0% and 95th percentage 19.4%) for hydraulic head. Large relative errors (>50%) in head measurement are thus obtained far from the pumping well, at short times T_k, where $h_n^{T_k}$ are close to zero. Log-conductivity measurements are made available at initial time $t = T_0 = 0$. The elements of vector $\mathbf{d}^{T_k}$, which in our examples contain head measurements at time T_k as defined in (10), coincide with h_n^{*,T_k} in (21). The corresponding covariance matrix of head measurement errors, $\mathbf{\Sigma}_{\varepsilon\varepsilon}^{T_k}$, is diagonal homoscedastic with diagonal entries equal to σ_{hE}^2. Entries H_{ij} of $\mathbf{H}$ are equal to 1 when d_i is a measurement of s_j and 0 otherwise.

3.1. ME-based EnKF

In the ME-based EnKF procedure the vector $\langle \mathbf{s}^{f,T_k} \rangle$ and the matrix $\mathbf{\Sigma}_{\mathbf{ss}}^{f,T_k}$ are set equal to second-order solutions of corresponding MEs. The following procedure is employed:

1. At initial time T_0, the measured log-conductivities, $\mathbf{Y}^*$, are projected via ordinary kriging onto the centroids of all grid elements using the generating variogram and parameters listed in Table 1 and the measurement error variance σ_{YE}^2.
2. First and second moments of initial heads, together with cross-covariances between h and Y, are obtained by solving steady state MEs [30] without pumping and with kriged Y values, and corresponding covariances, obtained at step 1 of the procedure.
3. The vector $\langle \mathbf{h} \rangle^{f,T_k}$ and the matrices $\mathbf{C}_h^{f,T_k}$ and $\mathbf{u}_{Yh}^{f,T_k}$ are computed to second-order in the standard deviation of Y by solving corresponding MEs (equations S1–S13 of the Supplementary material) with pumping using (a) at $k = 1$, kriged log-conductivities and covariances obtained in step 1 with initial head and second moments established at step 2; (b) at $k > 1$, mean log-conductivity $\langle \mathbf{Y} \rangle^{f,T_k}$ and covariance matrix $\mathbf{C}_Y^{f,T_k}$ updated at time T_{k-1} (equivalent to $\langle \mathbf{Y} \rangle^{u,T_{k-1}}$ and $\mathbf{C}_Y^{u,T_{k-1}}$, respectively) and initial conditions given by $\langle \mathbf{h} \rangle^{u,T_{k-1}}$, $\mathbf{C}_h^{u,T_{k-1}}$, $\mathbf{u}_{Yh}^{u,T_{k-1}}$.
4. The Kalman gain matrix $\mathbf{K}$ is evaluated according to (19).
5. The mean state vector and its covariance are updated on the basis of (17) and (18).

Steps 3–5 are repeated for each time period between measurements. For completeness, we include all relevant equations as an online supplement to this paper.

3.2. MC-based EnKF

In the MC-based EnKF procedure the vector $\langle \mathbf{s}^{f,T_k} \rangle$ and the matrix $\mathbf{\Sigma}_{\mathbf{ss}}^{f,T_k}$ are evaluated by Monte Carlo simulations as follows:

1. One generates a collection of log-conductivity realizations, $\mathbf{Y}_i$, $i = 1,\ldots,NMC$, conditioned on $\mathbf{Y}^*$ using the generating variogram and parameters listed in Table 1 and the measurement error variance σ_{YE}^2. Note that each $\mathbf{Y}_i$ is conditioned on different Y values, obtained by perturbing Y_m^* with a Gaussian noise having standard deviation σ_{YE}, as suggested by [5].

Table 1
Variogram input parameters, ratio between domain side and I_Y, sample variance, sill and integral scale obtained by fitting, using least squares, an exponential variogram model to the corresponding sample variogram.

Ref. case	Input parameters			Sample variance	Least squares fit	
	Sill	I_Y	Domain side / I_Y		Sill	I_Y
TC1	0.5	4.0	10	0.43	0.41	3.02
TC2	1.0	4.0	10	1.08	1.22	6.20
TC3	2.0	4.0	10	1.80	1.89	3.53
TC4	0.5	10.0	4	0.34	0.42	6.718
TC5	1.0	10.0	4	0.89	1.58	15.95
TC6	2.0	10.0	4	1.62	2.50	15.62
TC7	0.5	20.0	2	0.39	0.53	17.94
TC8	1.0	20.0	2	0.66	1.16	23.85
TC9	2.0	20.0	2	1.40	2.47	22.19

2. For each MC realization, $\mathbf{Y}_i$, one computes an initial head vector by solving the deterministic steady-state flow problem (1)–(5) without pumping.
3. For each $\mathbf{Y}_i$ and corresponding initial head one solves the deterministic transient flow problem (1)–(5) with pumping till time T_k at which new head measurements become available. The corresponding head, h_i^{f,T_k}, is computed (a) at $k = 1$ using $\mathbf{Y}_i$ from step 1 and initial head from step 2, and (b) at steps $k > 1$ using $\mathbf{Y}^{u,T_{k-1}}$ and initial head $\mathbf{h}^{u,T_{k-1}}$ updated at time T_{k-1}.
4. The mean and covariance are approximated by their sample counterparts

$$\langle \mathbf{s}^{f,T_k} \rangle \cong \boldsymbol{\mu}_s^{f,T_k} = \frac{1}{NMC} \sum_{i=1}^{NMC} \mathbf{s}_i^{f,T_k} \tag{22}$$

$$\boldsymbol{\Sigma}_{\mathbf{ss}}^{f,T_k} \cong \hat{\boldsymbol{\Sigma}}_{\mathbf{ss}}^{f,T_k} = \frac{1}{NMC-1} \sum_{i=1}^{NMC} (\mathbf{s}_i^{f,T_k} - \boldsymbol{\mu}_{\mathbf{s}}^{f,T_k})(\mathbf{s}_i^{f,T_k} - \boldsymbol{\mu}_{\mathbf{s}}^{f,T_k})^+ \tag{23}$$

1. At time T_k each vector $\mathbf{s}_i^{f,T_k}$ is updated on the basis of recently acquired measurements, in a manner similar to (17), through

$$\mathbf{s}_i^{u,T_k} = \mathbf{s}_i^{f,T_k} + \hat{\mathbf{K}}_{MC}(\mathbf{d}_i^{T_k} - \mathbf{H}\mathbf{s}_i^{f,T_k}) \quad i = 1, \ldots, NMC \tag{24}$$

where each vector $\mathbf{d}_i^{T_k}$ is obtained by adding white Gaussian noise with variance σ_{hE}^2 to the measurements σ_{hE}^2. The empirical Kalman gain matrix, $\hat{\mathbf{K}}_{MC}$, is obtained through (19) with $\boldsymbol{\Sigma}_{\mathbf{ss}}^{f,T_k}$ approximated by (23).

Steps 3–5 are repeated for each time period between measurements.

4. Results

In most previous applications of MC-based EnKF [11,18,24,40] the number *NMC* of Monte Carlo did not exceed a few hundred. Recognizing that *NMC* may have an impact on the results, we consider here a series of values *NMC* = 100; 500; 1000; 5000; 10,000; 50,000; 100,000. Here we show results corresponding to four selected scenarios. The complete set of results corresponding to all nine cases is available as Supplementary material online. Figs. 2 and 3, respectively, compare the spatial distributions of updated log-conductivity $\langle \mathbf{Y}^{u,T_k} \rangle$ with the corresponding reference fields, and corresponding estimation variances $\sigma_Y^{2\ u,T_k}$ (diagonal entries of $\mathbf{C}_Y^{u,T_k}$), at the final assimilation time ($T_k = 200.0$) for the selected reference cases obtained by ME- and MC-based EnKF. Values of $\langle \mathbf{Y}^{u,T_k} \rangle$ obtained with *NMC* < 1000 exhibit more pronounced spatial variability than those obtained from a larger number of *MC* realizations. Indeed, as $\langle \mathbf{Y}^{u,T_k} \rangle$ represents a relatively smooth estimate of $\mathbf{Y}$, spatial fluctuations are expected to diminish with increasing *NMC*. Results obtained with *NMC* > 10,000 are similar to those obtained with *NMC* = 10,000 for all cases examined and therefore not shown.

Estimation variance is seen to vary locally with *NMC*, due most likely to filter inbreeding. The problem seems to disappear at $NMC \geqslant 1000$ where the spatial distribution of MC-based variances is quite similar to that of their ME-based counterparts.

Figs. 4 and 5, respectively, show temporal behaviors of the average absolute difference, E_Y, between $\langle \mathbf{Y}^{u,T_k} \rangle$ and its reference value, $\mathbf{Y}_{ref}$, as well as the average estimation variance, V_Y, at all element centers, $\mathbf{x}_i$. As shown in [41], the quantity V_Y corresponds to the A-criterion of optimal design and provides a measure of conditional uncertainty associated with the estimated *Y* field. The two statistics are defined as

$$E_Y(t^*) = \frac{1}{N_Y} \sum_{i=1}^{N_Y} |\langle Y^{u,t^*}(\mathbf{x}_i) \rangle - Y(\mathbf{x}_i)_{ref}| \tag{25}$$

$$V_Y(t^*) = \frac{1}{N_Y} \sum_{i=1}^{N_Y} \sigma_Y^{2\ u,t^*}(\mathbf{x}_i) \tag{26}$$

Where $t^* = T_k/T_{\max}$, $T_{\max} = 200.0$, is normalized time (assimilation take place at $t^* = 0.050$, 0.075, 0.100, 0.125, 0.150, 0.250, 0.400, 0.500, 0.750, 1.00). E_Y and V_Y are seen to increase as the sill of the variogram increases and as I_Y decreases. The largest difference between MC-based values of E_Y and V_Y obtained with *NMC* = 100 and with *NMC* = 10,000 occurs in TC3 (Figs. 4b and 5b) where the sill is largest and the integral scale smallest. Fig. 4 shows that whereas E_Y tends to decrease with *NMC*, at large *NMC* its MC- and ME-based values are close. The only exception is TC9 (associated with the largest sill and I_Y, Fig. 4d), where the curve obtained with *NMC* = 10,000 lies slightly below that obtained with ME-based EnKF. In TC9, the relative difference between MC- and ME-based results varies between 18% at small t^* and 10% at large t^*. We ascribe

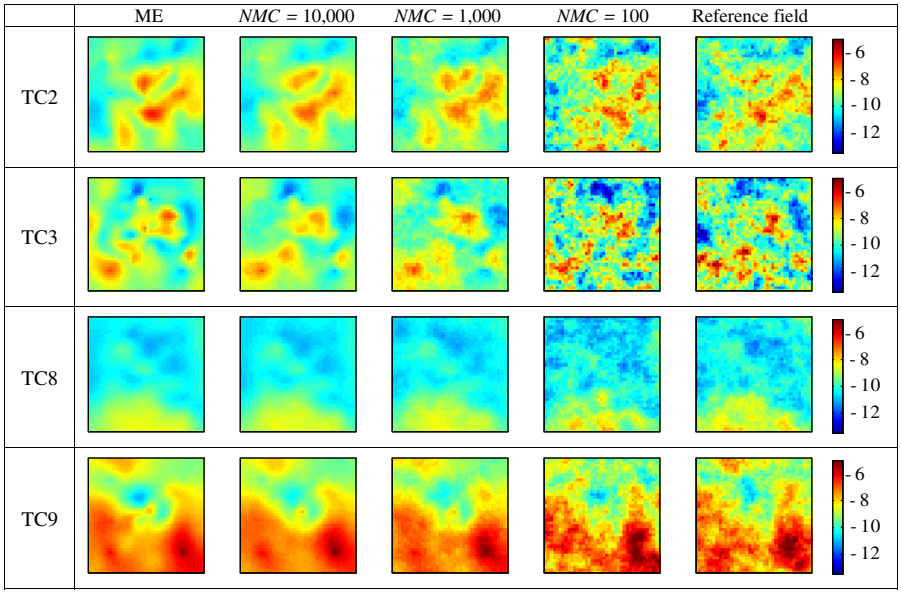

Fig. 2. Spatial distributions of $\langle \mathbf{Y}^{u,T_k} \rangle$ at $T_k = 200$ obtained by ME- and MC-based EnKF with diverse values of *NMC* and for selected test cases. Reference *Y* fields are also shown.

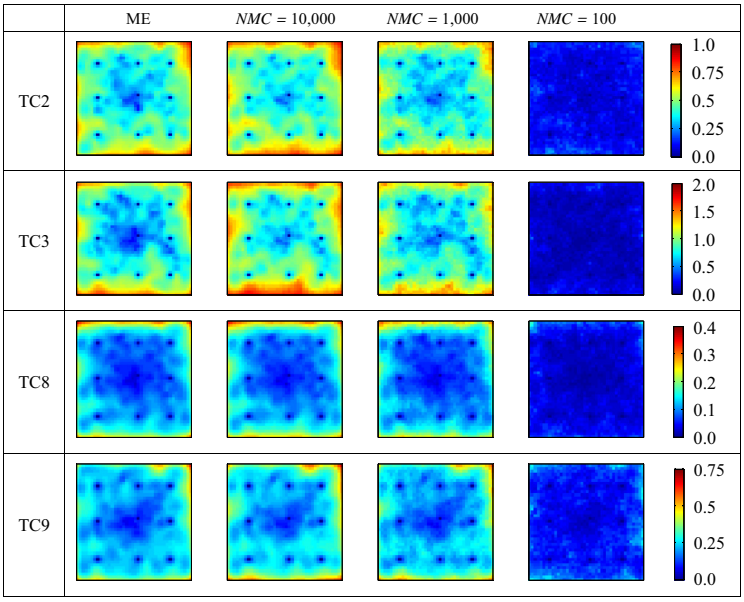

Fig. 3. Spatial distributions of $\sigma_Y^{2\ u,T_k}$ at $T_k = 200$ obtained by ME- and MC-based EnKF with diverse values of *NMC* and for the selected test cases depicted in Fig. 2.

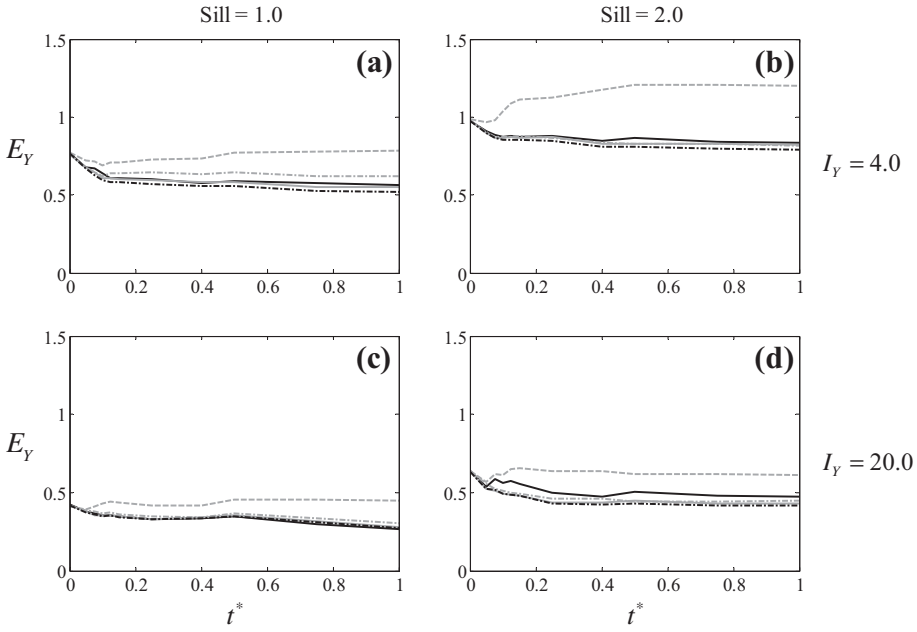

Fig. 4. E_Y versus t^* for the test cases depicted in Fig. 2. ME-based (solid black) and MC-based results with *NMC* = 100 (dashed gray), 500 (dashed-dotted gray), 1000 (solid gray), and 10,000 (dashed-dotted black) are reported.

this behavior to approximations required to close what would otherwise be exact moment equations. Inaccuracies associated with these approximations tend to increase with increasing values of I_Y relative to domain size.

Figs. 4 and 5 indicate that assimilations done with *NMC* = 100 are generally associated with (a) large E_Y values that tend to increase with time and (b) small V_Y values that tend to decrease with time. The two phenomena are symptomatic of filter inbreeding. Several authors [18,23,24] suggest to analyze the occurrence of filter inbreeding by plotting the ratio V_Y/MSE_Y versus time where

$$MSE_Y(t^*) = \frac{1}{N_Y}\sum_{i=1}^{N_Y}\left(\langle Y^{u,t^*}(\mathbf{x}_i)\rangle - Y(\mathbf{x}_i)_{ref}\right)^2 \tag{27}$$

Under ideal conditions, V_Y/MSE_Y should be 1 [23]. Here we explore this issue by considering also the quantity

$$P_{2\sigma_Y}(t^*) = \frac{1}{N_Y}\sum_{i=1}^{N_Y} H\{2\sigma_Y^{u,t^*}(\mathbf{x}_i) - |\langle Y^{u,t^*}(\mathbf{x}_i)\rangle - Y(\mathbf{x}_i)_{ref}|\} \tag{28}$$

where $H\{\bullet\}$ is the Heaviside step function, $P_{2\sigma_Y}$ representing percent reference values of Y lying inside a confidence interval of width equal to $\pm 2\sigma_Y^{u,t^*}(\mathbf{x}_i)$ about $\langle Y^{u,t^*}(\mathbf{x}_i)\rangle$. Analyses of the way V_Y/MSE_Y (Fig. 6) and $P_{2\sigma_Y}$ (Fig. 7) evolve with time lead to similar conclusions. When *NMC* < 1000, V_Y/MSE_Y and $P_{2\sigma_Y}$ decrease with time, exhibiting a distinct filter inbreeding effect. No such deterioration with time is exhibited by either MC-based results with *NMC* $\geqslant$ 1000 or

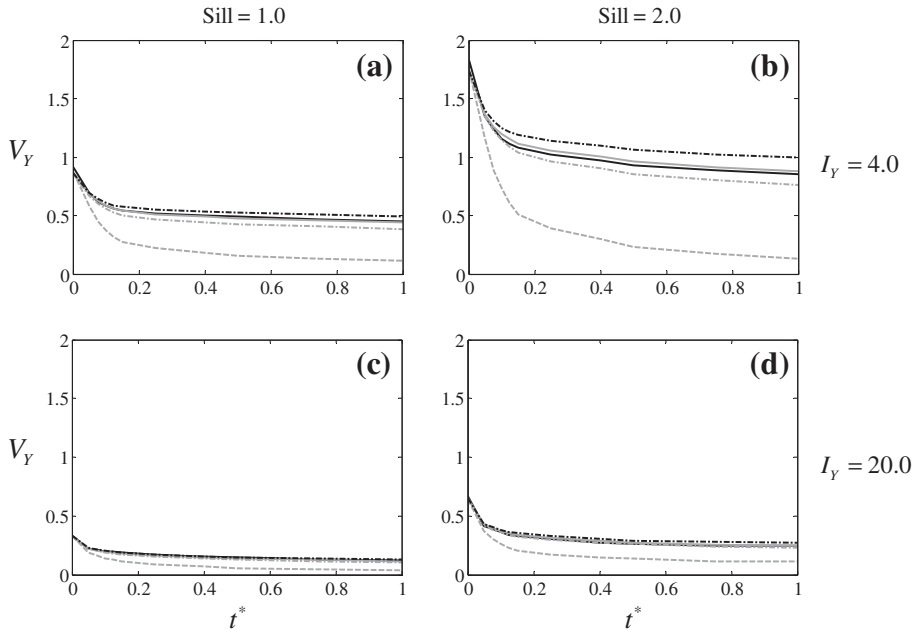

Fig. 5. $V_Y(t^*)$ versus t^* for the test cases depicted in Fig. 2. ME-based (solid black) and MC-based results with *NMC* = 100 (dashed gray), 500 (dashed-dotted gray), 1,000 (solid gray), and 10,000 (dashed-dotted black) are reported.

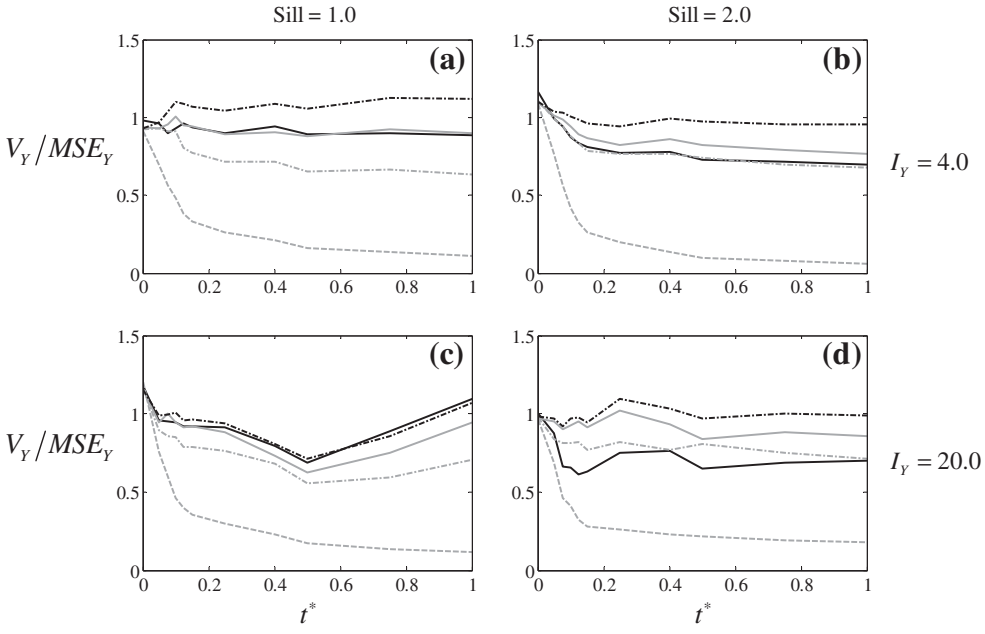

Fig. 6. Ratio between V_Y and MSE_Y versus t^* for the test cases depicted in Fig. 2. ME-based (solid black) and MC-based results with *NMC* = 100 (dashed gray), 500 (dashed-dotted gray), 1000 (solid gray), and 10,000 (dashed-dotted black) are reported.

by ME-based outcomes where V_Y/MSE_Y remains approximately constant and $P_{2\sigma_Y}$ larger than 90%. The only exception concerns ME-based results associated with TC9 (see Figs. 6d and 7d) where $P_{2\sigma_Y}$ is slightly smaller than 90% (≈88%). However, even here the ME-based values of V_Y/MSE_Y and $P_{2\sigma_Y}$ show no systematic decrease with time (as would happen in the presence of filter inbreeding) but instead diminish rapidly during the first assimilation period and then stay approximately constant. The rapid early decline is likely due to spurious updates caused by second-order approximation of the cross-covariance terms. In contrast to MC-based $P_{2\sigma_Y}$ which, at small *NMC*, drops down to below 40%, a steep decline in ME-based values is limited to early time.

Black dots in Fig. 8 indicate the spatial location of the reference values of Y lying, following the last assimilation period at $t^* = 1.0$, outside confidence intervals having widths equal to $\pm 2\sigma_Y^{u,t^*}(\mathbf{x}_i)$ about $\langle Y^{u,t^*}(\mathbf{x}_i)\rangle$. This confirms the poor quality of estimates obtained with *NMC* < 1000, even in the weakly heterogeneous test cases TC1, TC4 and TC7 (see also Supplementary material online). Remarkably, black dots in Fig. 8 corresponding to MC- (with *NMC* = 10,000) and ME-based filters have similar spatial distributions. It thus appears that the two EnKF approaches behave similarly in both a global (as observed in Figs. 4 and 5) and a local sense when *NMC* is sufficiently large. This behavior can be quantified by analyzing the percentage χ of cells in which reference

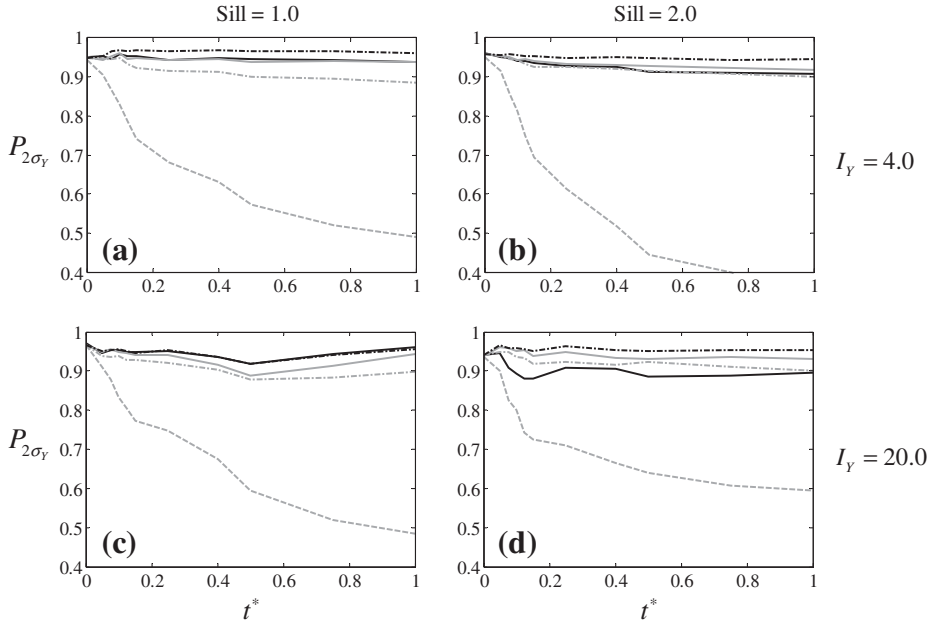

Fig. 7. $P_{2\sigma_Y}$ versus t^* for the test cases depicted in Fig. 2. ME-based (solid black) and MC-based results with *NMC* = 100 (dashed gray), 500 (dashed-dotted gray), 1000 (solid gray), and 10,000 (dashed-dotted black) are reported.

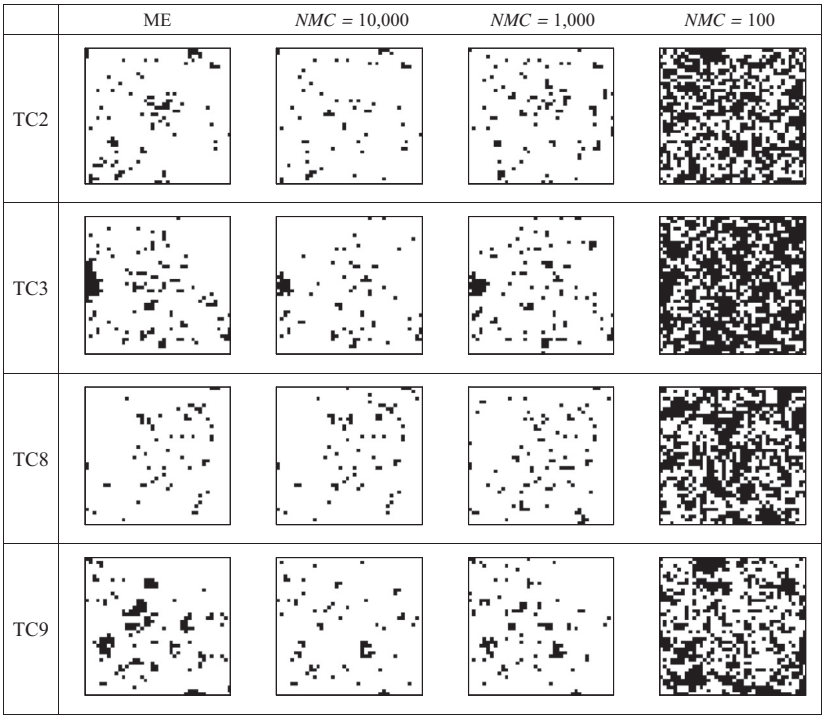

Fig. 8. Spatial distributions (black squares) of elements in which Y_{ref} lie outside confidence intervals of width ±2 $\sigma_Y^{u,T_k}(\mathbf{x}_i)$ about $\langle Y(\mathbf{x}_i)\rangle^{u,T_k}$ when $T_k = 200.0$ for the test cases depicted in Fig. 2.

values of Y lie within 95% confidence intervals around updated Y values in both the ME- and the MC-based solutions. As expected, this metric is seen to decrease as the number of MC realizations grows in all test cases. In case of the MC approach, average values of χ in the nine test cases are 94%, 93%, 91%, 87% and 48% for *NMC* = 10,000, 1000, 500, and 100, respectively.

Figs. 9 and 10 depict temporal behaviors of E_h and V_h, the hydraulic head analogues of E_h and V_Y in (25) and (26), defined as

$$E_h(t^*) = \frac{1}{N_h^*}\sum_{i=1}^{N_h^*}|\langle h^{u,t^*}(\mathbf{x}_i)\rangle - h(\mathbf{x}_i)_{ref}| \tag{29}$$

$$V_h(t^*) = \frac{1}{N_h^*}\sum_{i=1}^{N_h^*}\sigma_h^{2\,u,t^*}(\mathbf{x}_i) \tag{30}$$

where $\sigma_h^{2\,u,t^*}(\mathbf{x}_i)$ is the estimation variance of h at node $\mathbf{x}_i$ (i.e., a diagonal component of $\mathbf{C}_h^{u,t^*}$) and N_h^* is the number of nodes, N_h,

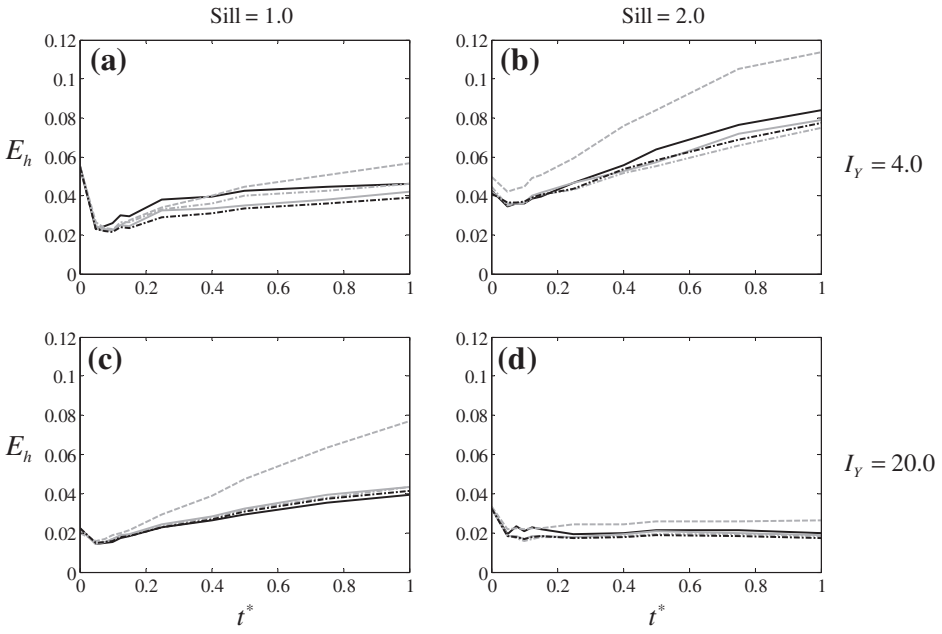

Fig. 9. $E_h(t^*)$ versus t^* for the test cases depicted in Fig. 2. ME-based (solid black) and MC-based results with *NMC* = 100 (dashed gray), 500 (dashed-dotted gray), 1000 (solid gray), and 10,000 (dashed-dotted black) are reported.

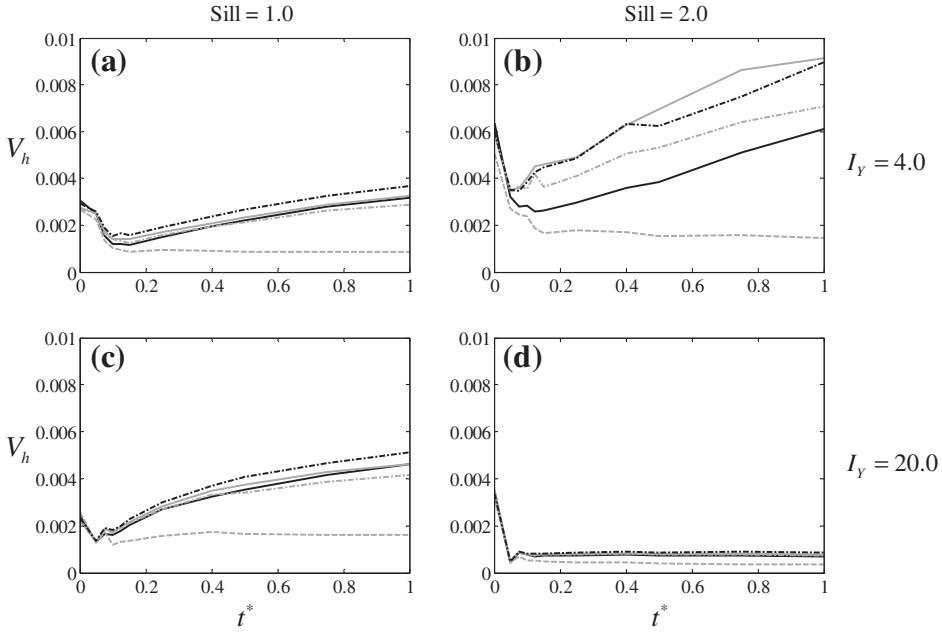

Fig. 10. $V_h(t^*)$ versus t^* for the test cases depicted in Fig. 2. ME-based (solid black) and MC-based results with *NMC* = 100 (dashed gray), 500 (dashed-dotted gray), 1000 (solid gray), and 10,000 (dashed-dotted black) are reported.

minus those located on Dirichlet boundaries and at the pumping well where, theoretically, $h \to -\infty$ due to the well's negligible radius. Fig. 9 shows that E_h decreases sharply at the first assimilation time, then increases with t^*. The largest rate of increase is associated with MC-based values obtained with *NMC* = 100. ME-based values of E_h are in general very close to MC-based values obtained with sufficiently large *NMC*. On the other hand, the monotonically decreasing temporal trend in V_Y is not mirrored by the mean estimation variance of h in Fig. 10. Instead, V_h in Fig. 10 decreases sharply during the first assimilation step and then increases with time. We attribute this to the combination of two contrasting effects: (a) the decrease of V_Y which is typically associated with the updating step, (b) the temporal increase or decrease (depending on location in the domain; see also Fig. 7 of [29] and results of [42]) in head variance during the forward steps. Effect (a) dominates during the first assimilation period, due to the high information content of the measurements (see also Figs. 4 and 5), causing V_Y to decrease initially with time. As time increases and pseudo-steady state conditions are approached, the conditioning head data become less informative (see also [27,42]). This is reflected in Fig. 4 where E_Y is seen to be almost constant at large values of t^*. Here effect (b) dominates, manifested by an increase in V_Y with time.

We close our analysis by plotting in Fig. 11 the temporal behavior of

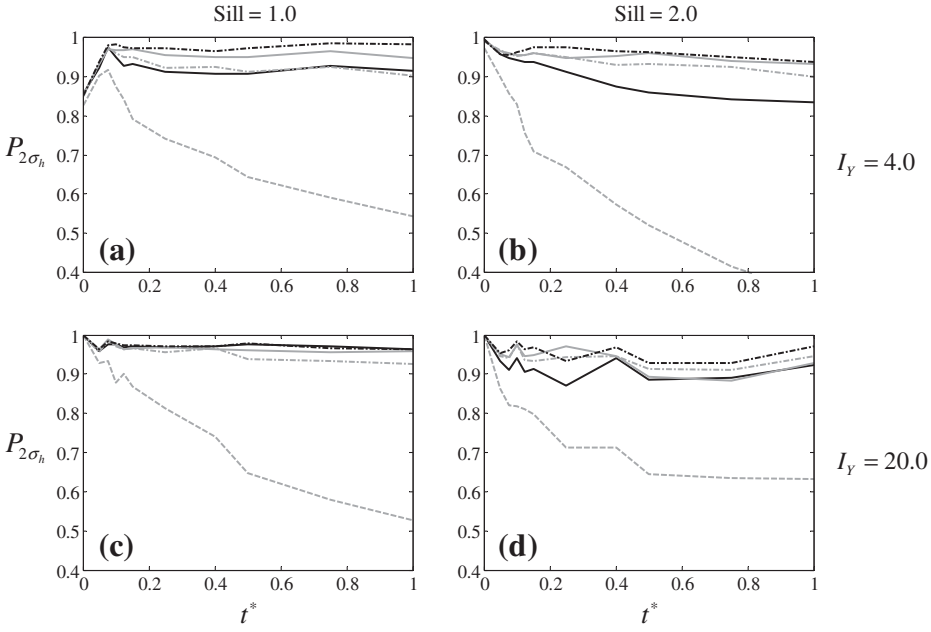

Fig. 11. $P_{2\sigma_h}$ versus t^* for the test cases depicted in Fig. 2. ME-based (solid black) and MC-based results with *NMC* = 100 (dashed gray), 500 (dashed-dotted gray), 1000 (solid gray), and 10,000 (dashed-dotted black) are reported.

$$P_{2\sigma_h}(t^*) = \frac{1}{N_h^*}\sum_{i=1}^{N_h^*} H\left\{2\sigma_h^{u,t^*}(\mathbf{x}_i) - |\langle h^{u,t^*}(\mathbf{x}_i)\rangle - h(\mathbf{x}_i)_{ref}|\right\} \tag{31}$$

representing percent reference h values lying inside a confidence interval of width equal to $\pm 2\sigma_h^{u,t^*}(\mathbf{x}_i)$ about $\langle h^{u,t^*}(\mathbf{x}_i)\rangle$. Fig. 11 confirms that filter inbreeding associated with small *NMC* impacts not only *Y* but also *h*.

Ye et al. [29] compared the computational time required by ME- and MC-based forward solutions of a transient groundwater flow problem similar to the one we analyze here and within a domain which is half the size of the one we consider. They found that, with *NMC* = 2,000, the ME-based method required one quarter to one half the computer time to evaluate mean heads and variances than did the MC-base approach. The authors computed head variances by solving an integral expression (their (47)) in the presence of deterministic sources, boundary and initial conditions, which does not require computing a complete head covariance matrix. To conduct a more comprehensive comparison with the MC-based approach, we opted in this work to compute the complete head covariance matrix at the end of each time interval $(T_{k-1}, T_k]$. Our EnKF updating step requires computing additional terms appearing in (S8)–(S10) and (S13) of the Supplementary material to account for randomness of the initial head condition. As recognized by [29], the computation of these terms can have a significant effect on computational time during the forward step. Indeed we find that, in our case, the ME- and MC-based approaches require 13,650 s and 0.375 × *NMC* s, respectively, of CPU time on 10 parallel 2.80 GHz Intel i7-860 processors. It follows that CPU time associated with ME-based EnKF is comparable to that associated with *NMC* ≈ 35,000 MC-based assimilations. Considering that in our test cases the MC approach converges within *NMC* ⩾ 10,000, which however requires a tenfold increase in *NMC* to ascertain convergence (i.e., *NMC* = 100,000 realizations are needed to ascertain convergence at *NMC* = 10,000), we conclude that ME-based EnKF constitutes a viable alternative to the traditional MC-based approach not only in terms of quality but also in terms of computational efficiency. To avoid bias in comparing the two methodologies, we applied both without resorting to covariance localization or inflation techniques. Both techniques have been noted to partially reduce filter inbreeding in the MC-based approach [17,23–26] and may thus help improve the quality of *Y* estimates for a given number of MC realizations.

5. Conclusions

The traditional Ensemble Kalman Filter (EnKF) method of data assimilation relies on Monte Carlo simulations and the computation of corresponding sample (not theoretical ensemble) moments. Elsewhere we proposed an alternative based on stochastic ensemble moment equations (MEs) of transient groundwater flow. Here we compared the performances and accuracies of the two methods on nine synthetic test cases involving two-dimensional transient groundwater flow toward a well pumping from a randomly heterogeneous confined aquifer subject to stochastic initial conditions and deterministic boundary conditions. The test cases differed in the variance and (integral) autocorrelation scale of log hydraulic conductivity. Our results confirm an earlier finding by others that a few hundred MC simulations are not enough to overcome filter inbreeding issues, which have a negative impact on the quality of log-conductivity estimates as well as predicted heads and associated estimation variances. ME-based EnKF, which obviates the need for repeated simulations, was demonstrated to be free of inbreeding issues.

The number of MC simulations required for accurate assimilation (on the order of 10,000 in our test cases), free of inbreeding effects, cannot be predicted *a priori*. To ascertain this number *a posteriori*, one must conduct ten times as many simulations (on the order of 100,000 in our study). Using 10 parallel 2.80 GHz Intel i7-860 processors, CPU times required for ME-based EnKF was equivalent to those required for about 35,000 MC runs. We thus conclude that ME-based EnKF constitutes a viable alternative to the traditional MC-based approach in terms of both quality and computational efficiency.

Acknowledgements

This work was supported in part through a contract between the University of Arizona and Vanderbilt University under the

Consortium for Risk Evaluation with Stakeholder Participation (CRESP), funded by the U.S. Department of Energy. Funding from MIUR (Italian ministry of Education, Universities and Research-PRIN2010-11; project: "Innovative methods for water resources under hydro-climatic uncertainty scenarios") is also acknowledged.

Appendix A. Supplementary data

Supplementary data associated with this article can be found, in the online version.

References

[1] Kalman RE. A new approach to linear filtering and prediction problems. J Basic Eng 1960;82(1):35–45. http://dx.doi.org/10.1115/1.3662552.
[2] Vrugt J, Diks CGH, Gupta HV, Bouten W, Verstraten JM. Improved treatment of uncertainty in hydrologic modeling: combining the strengths of global optimization and data assimilation. Water Resour Res 2005;41(1):W01017. http://dx.doi.org/10.1029/2004WR003059.
[3] Gelb A. Applied optimal estimation. The MIT Press; 1994.
[4] Evensen G. Sequential data assimilation with a nonlinear quasi-geostrophic model using Monte Carlo methods to forecast error statistics. J Geophys Res 1994;99(C5):10143–62. http://dx.doi.org/10.1029/94JC00572.
[5] Burgers G, van Leeuwen PJ, Evensen G. Analysis scheme in the ensemble Kalman filter. Mon Weather Rev 2008;126(6):1719–24. http://dx.doi.org/10.1175/1520-0493(1998) 126<1719:ASITEK>2.0.CO;2.
[6] Oliver DS, Chen Y. Recent progress on reservoir history matching: a review. Comput Geosci 2011;15(1):185–221. http://dx.doi.org/10.1007/s10596-010-9194-2.
[7] Liu H, Weerts AH, Clark M, Hendricks Franssen H-J, Kumar S, Moradkhani H, Seo D-J, Schwanenberg D, Smith P, van Dijk AIJM, van Velzen N, He M, Lee H, Noh SJ, Rakovec O, Restrepo P. Advancing data assimilation in operational hydrologic forecasting: progresses, challenges, and emerging opportunities. Hydrol Earth Syst Sci 2012;16(10):3863–87. http://dx.doi.org/10.5194/hess-16-3863-2012.
[8] McLaughlin DB. An integrated approach to hydrologic data assimilation: interpolation, smoothing, and filtering. Adv Water Resour 2002;25(8–12):1275–86. http://dx.doi.org/10.1016/S0309-1708(02)00055-6.
[9] Naevdal G, Johnsen LM, Aanonsen SI, Vefring EH. Reservoir monitoring and continuous model updating using ensemble Kalman filter. SPE J 2005;10(1):66–74. http://dx.doi.org/10.2118/84372-PA.
[10] Aanonsen SI, Nævdal G, Oliver DS, Reynolds AC, Vallès B. The ensemble Kalman filter in reservoir engineering – a review. SPE J 2009;14(3):393–412. http://dx.doi.org/10.2118/117274-PA.
[11] Chen Y, Zhang D. Data assimilation for transient flow in geologic formations via ensemble Kalman filter. Adv Water Resour 2006;29(8):1107–22. http://dx.doi.org/10.1016/j.advwatres.2005.09.007.
[12] Zhang D, Lu Z, Chen Y. Dynamic reservoir data assimilation with an efficient, dimension-reduced Kalman filter. SPE J 2007;12(1):108–17. http://dx.doi.org/10.2118/95277-PA.
[13] Zeng L, Chang H, Zhang D. A probabilistic collocation-based Kalman filter for history matching. SPE J 2011;16(2):294–306. http://dx.doi.org/10.2118/140737-PA.
[14] Zeng L, Shi L, Zhang D, Wu L. A sparse grid Bayesian method for contaminant source identification. Adv Water Resour 2012;37:1–9. http://dx.doi.org/10.1016/j.advwatres.2011.09.011.
[15] Ballio F, Guadagnini A. Convergence assessment of numerical Monte Carlo simulations in groundwater hydrology. Water Resour Res 2004;40:W04603. http://dx.doi.org/10.1029/2003WR002876.
[16] van Leeuwen PJ. Comment on "data assimilation using an ensemble Kalman filter technique". Mon Weather Rev 1999;127(6):1374–7. http://dx.doi.org/10.1175/1520-0493(1999) 127<1374:CODAUA>2.0.CO;2.
[17] Houtekamer PL, Mitchell HL. Data assimilation using an ensemble Kalman filter technique. Mon Weather Rev 1998;126(3):796–811. http://dx.doi.org/10.1175/1520-0493(1998) 126<0796:DAUAEK>2.0.CO;2.
[18] Hendricks Franssen HJ, Kinzelbach W. Real-time groundwater flow modeling with the ensemble Kalman filter: joint estimation of states and parameters and the filter inbreeding problem. Water Resour Res 2008;44:W09408. http://dx.doi.org/10.1029/2007WR006505.
[19] Wen X-H, Chen WH. Some practical issues on real-time reservoir updating using ensemble Kalman filter. SPE J 2007;12(2):156–66. 10.118/111571-PA.
[20] Hendricks Franssen HJ, Kaiser HP, Kuhlmann U, Bauser G, Stauffer F, Muller R, Kinzelbach W. Operational real-time modeling with ensemble Kalman filter of variably saturated subsurface flow including stream-aquifer interaction and parameter updating. Water Resour Res 2011;47:W02532. http://dx.doi.org/10.1029/2010WR009480.
[21] Wang X, Hamill TA, Whitaker JS, Bishop CH. A comparison of hybrid ensemble transform Kalman filter-optimum interpolation and ensemble square root filter analysis schemes. Mon Weather Rev 2007;135(3):1055–76. http://dx.doi.org/10.1175/MWR3307.1.
[22] Anderson JL. An adaptive covariance inflation error correction algorithm for ensemble filters. Tellus 2007;59A:210–24. http://dx.doi.org/10.1111/j.1600-0870.2006.00216.x.
[23] Liang X, Zheng X, Zhang S, Wu G, Dai Y, Li Y. Maximum likelihood estimation of inflation factors on error covariance matrices for ensemble Kalman filter assimilation. Q J R Meteorolog Soc 2012;138(662):263–73. http://dx.doi.org/10.1002/qj.912.
[24] Xu T, Gómez-Hernández JJ, Zhou H, Li L. The power of transient piezometric head data in inverse modeling: an application of the localized normal-score EnKF with covariance inflation in a heterogeneous bimodal hydraulic conductivity field. Adv Water Resour 2013;54:100–18. http://dx.doi.org/10.1016/j.advwatres.2013.01.006.
[25] Furrer R, Bengtsson T. Estimation of high-dimensional prior and posterior covariance matrices in Kalman filter variants. J Multivariate Anal 2007;98(2):227–55. http://dx.doi.org/10.1016/j.jmva.2006.08.003.
[26] Wang X, Bishop CH. A comparison of breeding and ensemble transform Kalman filter ensemble forecast schemes. J Atmos Sci 2003;60(9):1140–58. http://dx.doi.org/10.1175/1520-0469(2003) 060<1140:ACOBAE>2.0.CO;2.
[27] Panzeri M, Riva M, Guadagnini A, Neuman SP. Data assimilation and parameter estimation via ensemble Kalman filter coupled with stochastic moment equations of transient groundwater flow. Water Resour Res 2013;49(3):1334–44. http://dx.doi.org/10.1002/wrcr.20113.
[28] Tartakovsky DM, Neuman SP. Transient flow in bounded randomly heterogeneous domains: 1. Exact conditional moment equations and recursive approximations. Water Resour Res 1998;34(1):1–12. http://dx.doi.org/10.1029/97WR02118.
[29] Ye M, Neuman SP, Guadagnini A, Tartakovsky DM. Nonlocal and localized analyses of conditional mean transient flow in bounded, randomly heterogeneous porous media. Water Resour Res 2004;40(5):W05104. http://dx.doi.org/10.1029/2003WR00209.
[30] Guadagnini A, Neuman SP. Nonlocal and localized analyses of conditional mean steady state flow in bounded, randomly nonuniform domains: 2. Computational examples. Water Resour Res 1999;35(10):3019–39. http://dx.doi.org/10.1029/1999WR900159.
[31] Riva M, Sanchez-Vila X, Guadagnini A, De Simoni M, Willmann M. Travel time and trajectory moments of conservative solutes in two-dimensional convergent flows. J Contam Hydrol 2006;82:23–43. http://dx.doi.org/10.1016/j.jconhyd.2005.06.014.
[32] Riva M, Guadagnini L, Guadagnini A, Ptak T, Martac E. Probabilistic study of well capture zones distribution at the Lauswiesen field site. J Contam Hydrol 2006;88:92–118. http://dx.doi.org/10.1016/j.jconhyd.2006.06.005.
[33] Hendricks Franssen HJ, Alcolea A, Riva M, Bakr M, van der Wiel N, Stauffer F, Guadagnini A. A comparison of seven methods for the inverse modelling of groundwater flow. Application to the characterisation of well catchments. Adv Water Resour 2009;32(6):851–72. http://dx.doi.org/10.1016/j.advwatres.2009.02.011.
[34] Tarantola A. Inverse problem theory. Elsevier; 1987.
[35] Cohn SE. An introduction to estimation theory. J Meteorolog Soc Jpn 1997;75(IB):257–88.
[36] Woodbury AD, Ulrych TJ. A full-Bayesian approach to the groundwater inverse problem for steady state flow. Water Resour Res 2000;36(8):2081–93. http://dx.doi.org/10.1029/2000WR900086.
[37] Deutsch CV, Journel AG. GSLIB, geostatistical software library and user's guide. 2nd ed. New York: Oxford University Press; 1998 [p. 384. ISBN-10:0195100158].
[38] Jafarpour B, Tarrahi M. Assessing the performance of the ensemble Kalman filter for subsurface flow data integration under variogram uncertainty. Water Resour Res 2011;47:W05537. http://dx.doi.org/10.1029/2010WR009090.
[39] De Hoog FR, Knight JH, Stokes AN. An improved method for numerical inversion of Laplace transform. SIAM J Sci Stat Comput 1982;3(3):357–66.
[40] Schoeniger A, Nowak W, Hendricks Franssen HJ. Parameter estimation by ensemble Kalman filters with transformed data: approach and application to hydraulic tomography. Water Resour Res 2012;48:W04502. http://dx.doi.org/10.1029/2011WR010462.
[41] Nowak W. Measures of parameter uncertainty in geostatistical estimation and geostatistical optimal design. Math Geosci 2010;42(2):199–221. http://dx.doi.org/10.1007/s11004-009-9245-1.
[42] Riva M, Guadagnini A, Neuman SP, Bianchi Janetti E, Malama B. Inverse analysis of stochastic moment equations for transient flow in randomly heterogeneous media. Adv Water Resour 2009;32(10):1495–507. http://dx.doi.org/10.1016/j.advwatres.2009.07.003.